




# Synthesis and characterizations of (Mg, Co, Ni, Cu, Zn)O high-entropy oxides



Temesgen Debelo Desissa<sup>1</sup>  · Matusal Meja<sup>1</sup> · Dinsefa Andoshe<sup>1</sup> · Femi Olu<sup>3</sup> · Fekadu Gochole<sup>1</sup> · Gebisa Bekele<sup>1</sup> · Osman Ahmed Zelekew<sup>1</sup> · Tatek Temesgen<sup>2</sup> · Belay Brehane<sup>1</sup> · Kumsa D. Kuffi<sup>4</sup> · Tadele Hunde<sup>1</sup>

Received: 6 May 2021 / Accepted: 6 July 2021

Published online: 09 July 2021

© The Author(s) 2021 

## Abstract

High-temperature structural ceramic materials require stability in terms of thermal and mechanical properties. High entropy oxides (HEOs) are among the emerging novel family of advanced ceramic materials with peculiar functional properties. However, their thermal stabilities and mechanical properties are not well investigated. In this work, HEO systems were synthesized from binary oxides of MgO, CoO, NiO, CuO, and ZnO using solid-state reaction method at high temperature, after obtaining the individual oxides through co-precipitation methods. The phase purity of as-synthesized and sintered samples was characterized using X-ray powder diffraction, while the microstructural investigation was performed using Scanning electron microscopy. Mechanical property of the sintered samples at different sintering times and temperatures was investigated and the sample sintered at a sintering temperature of 1200 °C for 15 h sintering time showed a maximum Vickers hardness of about 16 GPa. This result is comparable with some of the hard ceramic materials, and therefore the materials could be a potential candidate for structural applications.

## 1 Introduction

High-entropy materials (HEMs) can be regarded as any solid solution materials that are comprised of quasi-equimolar multicomponent [1]. HEMs have a broad range of applications in the field of materials science due to their unique and novel characteristics [2–6]. This class of materials may provide an opportunity for developing advanced and innovative materials, thereby breaking the limitations of traditional materials properties [7, 8]. Among the HEMs, high-entropy alloys (HEAs) were reported in 2004 [4] and these materials contain five or more principal elements in near to equiatomic molar ratios. The concept of multicomponent entropy-stabilized solid solutions can be extended

to High-entropy metallic glass (HEMGs) Nanoparticles (NPs), High-entropy sulfides (HESs), High-entropy borides (HEBs), High-entropy carbides (HECs), High-entropy nitrides (HENs), and High-entropy oxides (HEOs) [8, 8–13].

Metal oxides play a very important role in today's technological advancements such as energy harvesting and production, photo-catalysis, high-temperature contact materials, and environmental pollution preventions supported by nanotechnology [14–18]. High entropy oxides (HEOs) are established from these metal oxides and are entropy-stabilized solid-solutions where nearly equimolar multi-components of the oxides are brought into a single-phase material [19–22] through thermodynamic stabilizations [23]. Single-phase HEOs contain five or more cations

✉ Temesgen Debelo Desissa, [temesgen.debelo@astu.edu.et](mailto:temesgen.debelo@astu.edu.et) | <sup>1</sup>Department of Materials Science and Engineering, School of Mechanical, Chemical and Materials Engineering (SoMCME), Adama Science and Technology University (ASTU), 1888 Adama, Ethiopia. <sup>2</sup>Department of Chemical Engineering, School of Mechanical, Chemical and Materials Engineering (SoMCME), Adama Science and Technology University (ASTU), 1888 Adama, Ethiopia. <sup>3</sup>Faculty of Materials Science and Engineering, Jimma Institute of Technology, Jimma University, 378 Jimma, Ethiopia. <sup>4</sup>School of Chemical and Bioengineering, Addis Ababa Institute of Technology, Addis Ababa University, 1176 Addis Ababa, Ethiopia.



so that the configurational entropy,  $\Delta S_{config} \geq 1.5R$  per mole [24]. Moreover, the molar configurational entropy ( $\Delta S_{config}$ ) of HEOs can be calculated as follows:

$$\Delta S_{config} = -R \left[ \left( \sum_{i=1}^N x_i \ln x_i \right)_{\text{cation site}} + \left( \sum_{j=1}^M x_j \ln x_j \right)_{\text{anion site}} \right] \quad (1)$$

where  $x_i$  and  $x_j$  represent the mole fraction of elements present in the cation and anion sites respectively, and  $R$  is the universal gas constant ( $R=8.314$  J/mole K) [20, 25]. The anion site contribution is expected to have only a minor effect on configurational entropy, due to the presence of only one anion that does not alter during the mixing of the HEO systems. However, the cation sub-lattice will change the mixing process for phase stabilization of the materials. As a result, the  $\Delta S_{config}$  contribution of oxygen sub-lattice would remain ideally zero and that of the entire system can be considered to be mainly dependent on the cation sub-lattice [26, 27]. Entropy stabilized oxide materials [2, 3] can be classified as low, medium, and high entropy oxides, if their  $\Delta S_{config}$  values are  $< 1R$ ,  $1.5R > \Delta S_{config} \geq 1$ , and  $\geq 1.5R$ , respectively and, therefore HEOs have a  $\Delta S_{config}$  of  $\geq 1.5R$ .

HEO materials have ample structural diversity with exciting properties, which form a promising novel class of materials for a broad range of applications such as structural to functional materials. For instance, a recent study by Banerjee et al. [28] showed that HEOs can be a potential candidate for thermoelectric materials for energy harvesting as these materials exhibited ultralow thermal conductivities at different temperature ranges. A study by Edalati et al. [29] on the photocatalytic properties of HEOs for hydrogen evolution, on the other hand, showed an appreciable light absorbance in the visible-light region for water splitting. Bérardan et al. [30] also reported that HEOs can exhibit colossal dielectric constant for applications as large- $k$  dielectric materials. Moreover, Wang et al. [31] studied HEOs for applications as anode materials for Li-ion batteries. They found out that HEOs exhibited promising electrochemical performance properties and can be potential candidate materials as electrodes for use in Li-ion batteries. Mechanical properties of these HEOs in relation to microstructural evolutions in relation to cheap synthesis techniques, however, are not well investigated. Therefore, in this work, HEOs materials were synthesized from MgO, CoO, NiO, CuO, and ZnO through environmentally friendly and cheap synthesis method, followed by materials characterizations and measurements of mechanical property through the Vickers hardness test on sintered pellets of HEOs.

## 2 Materials and methods

### 2.1 Materials

#### 2.1.1 Chemical reagents

Chemicals such as Magnesium Nitrate Hexahydrate ( $\text{Mg}(\text{NO}_3)_2 \cdot 6\text{H}_2\text{O}$ ) (Loba Chem, 99%), Cobalt Nitrate Hexahydrate ( $\text{Co}(\text{NO}_3)_2 \cdot 6\text{H}_2\text{O}$ ) (Sigma Aldrich, 99%), Nickel Nitrate Hexahydrate ( $\text{Ni}(\text{NO}_3)_2 \cdot 6\text{H}_2\text{O}$ ) (Loba Chem, 99%), Copper Sulfate Pentahydrate ( $\text{CuSO}_4 \cdot 5\text{H}_2\text{O}$ ) (Loba Chem, 99%), and Zinc Nitrate Hexahydrate ( $\text{Zn}(\text{NO}_3)_2 \cdot 6\text{H}_2\text{O}$ ) (Sigma Aldrich, 99%) were used in this work. The corresponding high entropy oxide was synthesized from Magnesium oxide (MgO), Cobalt oxide (CoO), Nickel oxide (NiO), Copper oxide (CuO), and Zinc oxide (ZnO) after these binary oxides were obtained from their respective precursors mentioned above. Sodium hydroxide (NaOH) was used as precipitating/mineralizer agent. Distilled water and ethanol were used as a solvent.

### 2.2 Methods

#### 2.2.1 Synthesis of binary oxides

In the present work, initially, the individual metallic oxides such as MgO, CoO, NiO, CuO, and ZnO were synthesized using a co-precipitation method from their respective precursors [23]. Figure 1 below illustrates the overall procedures for the synthesis of individual metallic oxide particles.

**2.2.1.1 Magnesium oxide (MgO)** MgO was synthesized using magnesium nitrate hexahydrate ( $\text{Mg}(\text{NO}_3)_2 \cdot 6\text{H}_2\text{O}$ ) as a source of  $\text{Mg}^{2+}$  ions, and a precipitating agent of sodium hydroxide (NaOH) was used as  $\text{OH}^-$  ions source [32]. In a typical reaction process for the synthesis of MgO, 0.2 M of magnesium nitrate solution was prepared by using 100 ml of distilled water as a solvent, followed by stirring using a magnetic stirrer at room temperature for about 45 min to obtain a homogeneous solution. Then, 2MNaOH solution was added dropwise into the magnesium nitrate solution with continuous stirring until the pH value reached about 9. The white precipitate of magnesium hydroxide was formed after a few minutes, and the stirring was continued for about 1 h. The obtained precipitate was centrifuged and washed with distilled water and ethanol to remove the residuals, followed by drying in an oven at 100 °C for 3 h. Finally, the obtained powder was calcined at 600 °C for 4 h in a muffle furnace to get the desired MgO powders.

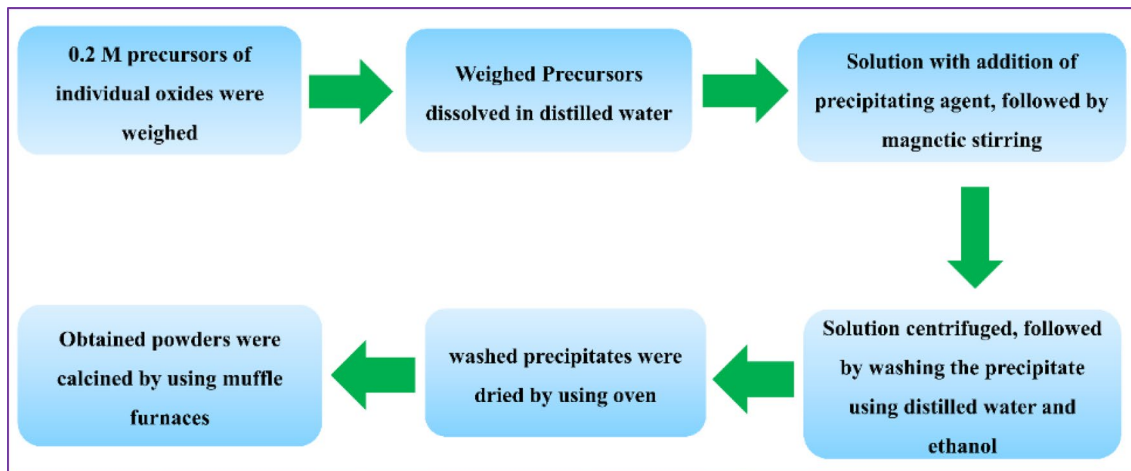


Fig. 1 Flow chart of synthesis procedures of individual metallic oxides

**2.2.1.2 Cobalt oxide (CoO)** To obtain Cobalt oxide in its binary oxidation state, i.e.,  $\text{Co}^{2+}$ , initially about 5.8 g of Cobalt Nitrate hexahydrate was dissolved in 100 ml distilled water, followed by stirring for about 45 min at room temperature to obtain 0.2 M solution [33]. Simultaneously, 2 M of NaOH was added to the solution of cobalt nitrate dropwise under vigorous stirring until the pH value of the solution reached 9. When the pH value of the solution was achieved, a pink color precipitate was formed. Then, the solution was subjected to heating at a temperature of 60 °C and kept under constant stirring for 2 h. A dark brown colored precipitate was formed at the bottom of the beaker. The obtained precipitate was filtered and washed several times by using distilled water and ethanol. The resultant product was dried in the oven at 100 °C for 5 h, and it was calcined at 1000 °C with a rate of 10 °C/min for 3 h in a high-temperature box furnace to obtain cobalt oxide (CoO) powder. Consequently, the calcined sample was quenched from 1000 °C to room temperature very quickly to avoid the formation of  $\text{Co}_3\text{O}_4$  [34].

**2.2.1.3 Nickel oxide (NiO)** NiO particles were synthesized from the precursor of  $\text{Ni}(\text{NO}_3)_2 \cdot 6\text{H}_2\text{O}$  using NaOH as a pH adjuster. For the typical experimental procedure, about 0.2 M of  $\text{Ni}(\text{NO}_3)_2 \cdot 6\text{H}_2\text{O}$  was dissolved in 100 ml of distilled water under constant stirring for about 1 h. Meanwhile, 2 M of NaOH was added to the  $\text{Ni}(\text{NO}_3)_2 \cdot 6\text{H}_2\text{O}$  solution dropwise with continuous stirring until the pH value of the solution reached 10 [35]. This solution was subjected to constant stirring at a temperature of around 80 °C for about 4 h. After completion of the reaction, the green-colored precipitate was obtained, and it was thoroughly washed with distilled water and ethanol to remove residuals. The precipitate was dried at 80 °C for 12 h and crushed

into a fine powder using agate mortar. Finally, the powder was calcined at 600 °C for 4 h using a muffle furnace.

**2.2.1.4 Copper oxide (CuO)** To synthesis CuO particles, about 4.994 g of  $\text{CuSO}_4 \cdot 5\text{H}_2\text{O}$  was dissolved in 100 ml of distilled water to obtain a 0.2 M solution, followed by constant stirring for 30 min. Then, 2 M of NaOH was added drop-wise to the solution of the  $\text{CuSO}_4 \cdot 5\text{H}_2\text{O}$  solution by touching the walls of the vessel under vigorous stirring until the pH value of a solution reached 13. Then, gradually, a black-colored precipitate was formed, and the reaction was allowed to proceed for 2 h under constant stirring at a temperature of 32 °C. Then the solution was allowed to settle overnight, and supernatant solutions were discarded carefully. The obtained precipitate was centrifuged and washed several times with distilled water and ethanol. Finally, the washed precipitate was dried at 80 °C for 12 h, followed by calcination at 500 °C for 4 h using a muffle furnace [36].

**2.2.1.5 Zinc oxide (ZnO)** ZnO particles were synthesized using  $\text{Zn}(\text{NO}_3)_2 \cdot 6\text{H}_2\text{O}$  precursor materials and NaOH solution as a pH adjuster. Briefly, 5.948 g of  $\text{Zn}(\text{NO}_3)_2 \cdot 6\text{H}_2\text{O}$  was dissolved in 100 ml distilled water and stirred for 45 min. The solution temperature was increased and when it reached about 70 °C, drop-wise addition of 3 M NaOH was performed until the pH of the solution reached 10. Then, stirring continues for about 2 h and after completion of the reaction, a milky white precipitate was formed. The solution was kept overnight so that the precipitate can coagulate and settle to the bottom of the solution. The resulting white precipitate was separated by centrifuge and washed several times with distilled water and ethanol. The filtered precipitate was dried at 80 °C for 8 h, fol-

lowed by calcination at a temperature of 500 °C for 2 h in a muffle furnace [37].

### 2.2.2 Synthesis of high entropy oxide (HEO)

HEO samples were synthesized from the obtained individual binary oxides using conventional solid-state reactions at high temperatures. Based on the literature [38], the starting individual binary oxide powder in stoichiometric amounts with specific equimolar amounts of the metallic oxides was calculated and weighed using an analytical precision balance. The corresponding composition, molar amount, and measured mass of binary oxides are summarized in Table 1.

The weighed powders were mixed in high-density polyethylene (HDPE) cylindrical jar using ethanol solvent and subjected to mechanical mixing using ball milling at around 320 rpm for 10 h using 2 mm and 5 mm diameters of zirconia balls as milling media [39]. To ensure adequate mixing and for attaining uniform dispersions of the constituent oxides, all batches of HEO pre-alloyed powder were milled for more than 10 h. After ball milling, the mixture was filtered and dried at a temperature of 100 °C for 5 h in a forced convection drying oven for removal of the solvent. The dried powder was air-cooled to room temperature and grounded using an alumina pestle and mortar to obtain fine particles of the pre-alloyed or pre-mixed samples.

Then, in the first part, the dried fine powder of the mixture was calcined at temperatures of 750 °C, 800 °C, 850 °C, 900 °C, 950 °C, 1000 °C, 1050 °C, and 1100 °C, using a high-temperature muffle furnace with the heating rate of 10 °C/min for 3 h holding time at the desired temperatures. Then, to avoid phase separation of the mixture, all batches of samples were quickly removed from the furnace, followed by quenching to room temperature in the air.

In the second part, the well-mixed un-calcined fine powders were separated into several samples with about 3.5 g per sample and then pressed into pellets with a 20 mm diameter pressing mold, using a uniaxial hydraulic mounting press at a pressing pressure of 45 MPa with

30 min of compaction time. Then, the obtained pellets were subjected to conventional sintering at temperatures of 900 °C, 1000 °C, 1100 °C, and 1200 °C with a heating rate of 10 °C/min at each sintering temperatures. The sintered pellets were air quenched to room temperature by directly taking from the furnace to avoid phase separations.

### 2.3 Characterization and performance evaluation methods

The crystal structure and phase purity of as-synthesized individual binary oxides (MgO, CoO, NiO, CuO, and ZnO) powder samples, as well as the calcined powders and sintered HEOs samples, were characterized by using an X-ray Diffraction instrument (XRD) (XRD-7000S Shimadzu) with Cu K $\alpha$  radiation, (Cu-K $\alpha$  radiation  $\lambda = 1.5406 \text{ \AA}$ ) using the operating voltage of 40 kV, a current of 30 mA, over the diffraction angle ( $2\theta$ ) range between 10° and 80°. The microstructure and elemental composition analysis of the samples were characterized using Scanning Electron Microscope (SEM) and Energy Dispersive X-ray spectroscopy (EDX) (COXIEM-30) with the operating voltage of 20 keV. The thermal behavior of HEO samples was investigated using simultaneous differential thermal analysis and thermo-gravimetric analysis (DTA–TG) measurement (DTG-60H Shimadzu) from room temperature to 1000 °C, using  $\alpha\text{-Al}_2\text{O}_3$  as reference. The mechanical property of the samples sintered at different sintering temperatures and sintering time was evaluated using Vickers hardness testing machine (HVS-50) with a testing standard of ASTM C1327.

## 3 Results and discussion

Figure 2 illustrates the XRD pattern of individual oxides confirming that the synthesized individual oxides exhibited a single phase. The synthesized MgO showed cubic crystal structure with corresponding peaks at a  $2\theta$  of 36.89°, 42.86°, 62.22°, 74.59°, and 78.52°, respectively, corresponding to (111), (200), (220), (311), and (222) crystallographic planes, which is in agreement to JCPDS Card No. 45–0946 with a space group of  $Fm\text{-}3m$  [40]. From the XRD pattern of CoO, all the major peaks have occurred at a  $2\theta$  of 36.25°, 42.15°, 61.05°, 73.10°, and 77° which correspond to crystallographic planes of (111), (200), (220), (311), and (222), respectively. The crystal is a rock-salt structure with the space group of  $Fm\text{-}3m$  in agreement to JCPDS Card No. 48–1719 [41]. The XRD patterns of NiO, as shown in Fig. 2, exhibited diffraction peaks at a  $2\theta$  of 37.16°, 43.22°, 62.75°, 75.27°, and 79.24° corresponding to (111), (200), (220), (311) and (222) crystal planes, respectively, with the cubic crystal structure (lattice constant of 0.418 nm) and space

**Table 1** Measured amounts of each oxide component for the synthesis of entropy stabilized oxide

Binary oxides	Molar amount (mole)	Mass of each component (g)
MgO	0.02	0.806
CoO	0.02	1.499
NiO	0.02	1.494
CuO	0.02	1.591
ZnO	0.02	1.628

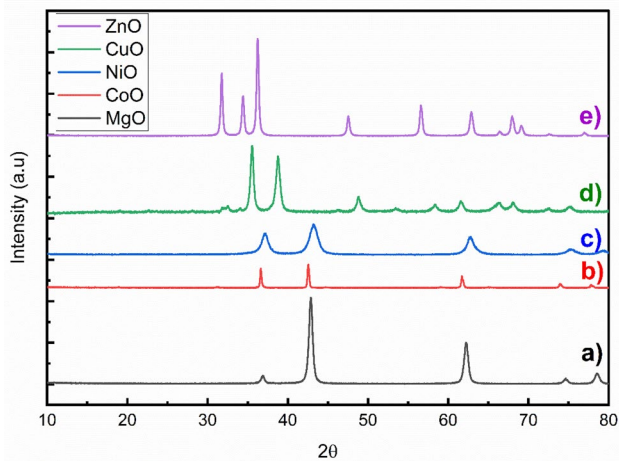


**Fig. 2** XRD patterns of individual binary oxides (a) MgO, (b) CoO, (c) NiO, (d) CuO, and (e) ZnO

group of  $Fm-3m$  (JCPDS Card No. 47–1049) [42]. The peaks from the XRD patterns of CuO particles are at  $2\theta$  of  $32.6^\circ$ ,  $35.5^\circ$ ,  $38.8^\circ$ ,  $48.8^\circ$ ,  $53.5^\circ$ ,  $58.5^\circ$ ,  $61.8^\circ$ ,  $66.3^\circ$ ,  $68.3^\circ$ ,  $72.5^\circ$ , and  $75.2^\circ$ , which correspond to (110), (-111), (111), (-202), (020), (202), (-113), (-311), (220), (311), and (004) crystallographic planes, respectively. The crystal structure of CuO is cubic in the monoclinic phase with a space group of  $C2/c$  and agrees with JCPDS card no.48–1548) [43]. Finally, ZnO XRD diffraction peaks were observed at a  $2\theta$  of  $31.77^\circ$ ,  $34.42^\circ$ ,  $36.26^\circ$ ,  $47.54^\circ$ ,  $56.60^\circ$ ,  $62.87^\circ$ ,  $66.39^\circ$ ,  $67.95^\circ$ ,  $69.10^\circ$ ,  $72.54^\circ$  and  $76.96^\circ$  corresponding to (100), (002), (101), (102), (110), (103), (200), (112), (201), (004) and (202) crystallographic planes, respectively. The sample showed a Wurtzite crystal structure with a space group of  $P63mc$  and agrees with JCPDS Card No. 36–1451[44].

A TGA analysis was performed on the mixture of powder precursors of binary oxides to determine the range of temperatures in which the HEO phases start to form. Figure 3 shows the TGA of the HEO powder precursors and three main endothermic peaks are observed from the plot, i.e.,  $\alpha$ ,  $\beta$ , and  $\delta$  peaks with three steps of decompositions. The first step ( $\alpha$  region) was observed at an endothermic peak temperature of around  $79^\circ\text{C}$  with a corresponding weight loss of about 25 wt. %, which could be related to the evaporation of residual water molecules adsorbed on the surface of the particles of the sample.

The second step ( $\beta$  region) occurred at a temperature of around  $286^\circ\text{C}$  representing the evolution of crystallization water and carbon dioxide with the corresponding weight loss of about 0.246%. Within these temperature ranges, hydroxides and basic carbonates of the different metals used in this work could undergo decomposition [45]. In the third step ( $\delta$  region) decomposition, a pronounced endothermic peak is observed at about  $744^\circ\text{C}$  with the

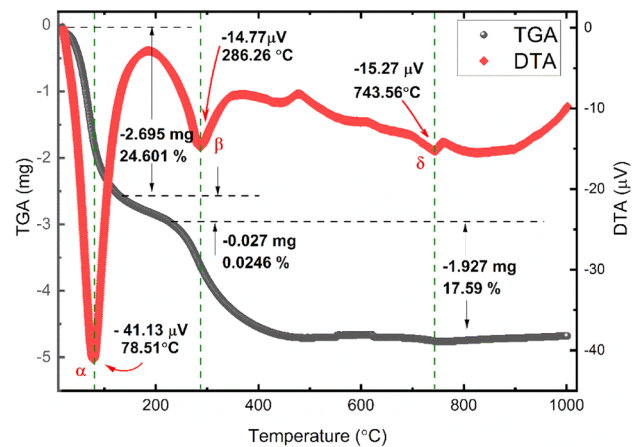


**Fig. 3** TG-DTA plots of HEO powder precursors

corresponding weight loss of about 18%, which could be attributed to the decomposition of  $\text{Co}_3\text{O}_4$  to CoO with the simultaneous evolution of  $\text{O}_2$  to maintain stoichiometry [46]. As a result of these three steps of decompositions, a total weight loss of about 43% was observed and this may be attributed to the combination of multi-components of the HEO systems. Moreover, it is interesting to observe that, there is no considerable loss of weight observed from the sample above  $750^\circ\text{C}$  and this could be the point at which the HEO starts to form, and the calcination temperatures were limited to above a temperature of  $750^\circ\text{C}$  to observe the evolution of the single phase formation of HEOs.

Figure 4 is the XRD pattern of the HEOs of as-synthesized near to equimolar compositions of  $(\text{Mg}_{0.2}\text{Co}_{0.2}\text{Ni}_{0.2})$

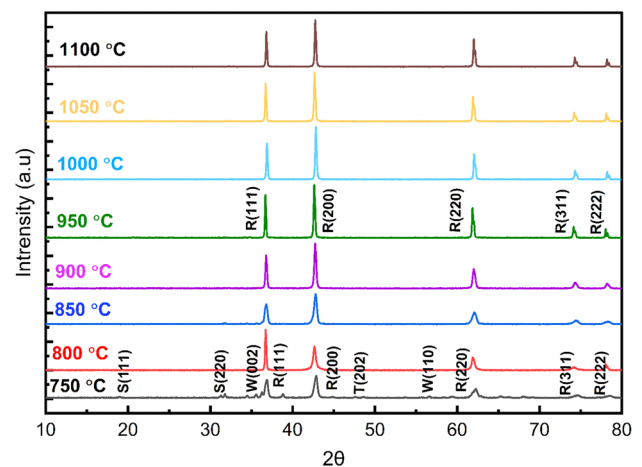


**Fig. 4** XRD patterns for the entropy-stabilized oxide of an equimolar mixture of MgO, CoO, NiO, CuO, and ZnO. The patterns were collected from the powder form of a mixture, calcined at the temperature in the range of  $750^\circ\text{C}$ – $1100^\circ\text{C}$  with  $50^\circ\text{C}$  increments: Rock-salt (R), Wurtzite (W), Tenorite (T), and  $\text{Co}_3\text{O}_4$  spinel (S)

$\text{Cu}_{0.2}\text{Zn}_{0.2}\text{O}$  powders. Based on the TGA result, the calcination temperatures ranged from 750 °C to 1100 °C with 50 °C intervals to determine the single-phase formation temperature of HEO from the present binary oxides. At a lower temperature regime of around 750 °C, the powders did not form a single-phase as different peaks for the individual oxides phases were observed, namely Rock-salt (R), Tenorite (T), Wurtzite (W), and  $\text{Co}_3\text{O}_4$  spinel (S) structure. Then, the fraction of Wurtzite ( $\text{ZnO}$ ,  $P63mc$ ), Tenorite ( $\text{CuO}$ ,  $C2/c$ ), and  $\text{Co}_3\text{O}_4$  spinel ( $Fd-3m$ ) phases were reduced with an increase in calcination temperature to 900 °C and above. This is due to the partial conversion to the rock-salt structure and at the same time, the  $\text{Co}_3\text{O}_4$ -like spinel phase disappears due to its complete decomposition into  $\text{CoO}$ .

The XRD diffraction patterns of the major peaks of a sample calcined at 950 °C can be easily indexed with a single-phase, rock-salt structure with the space group of  $Fm-3m$  (standard XRD patterns of HEO systems) [39]. According to the standardized PDF cards, the XRD patterns of the sample calcined at 950 °C occurred at a  $2\theta$  values of 36.80°, 42.75°, 62.01°, 74.31°, and 78.19° which can be indexed to (111), (200), (220), (311), and (222) crystallographic planes, respectively, in an agreement to the rock salt FCC crystal structure [27]. Increasing the calcination temperature above 950 °C causes a marginal shift of the identified XRD peaks towards the higher  $2\theta$  and the peak splitting was observed, as shown in Fig. 5 on the diffraction peaks of (111) and (220) crystallographic planes. This

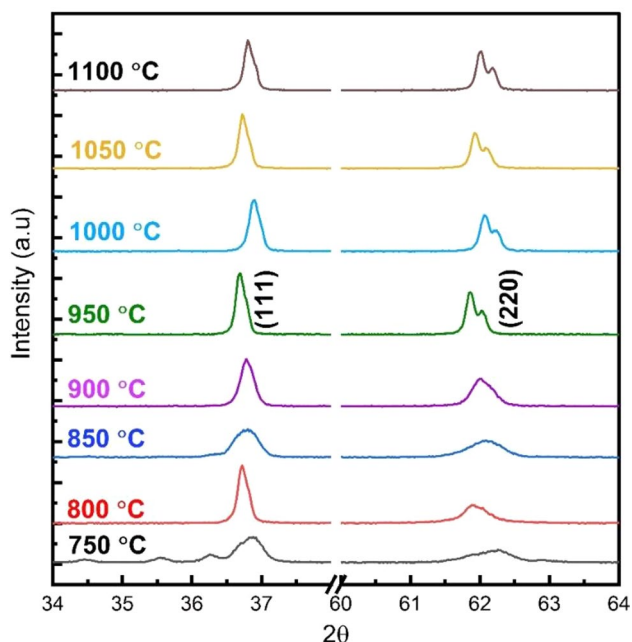


**Fig. 5** Expanded view of XRD pattern of HEO for (a) (111) peak from 30°–40° and (b) (220) peak from 60°–64° to observe the peak evolution with changing temperature

could be attributed to the immiscibility and alteration of cations in the sub-lattice of HEOs leading to the reverse phase transformation of the systems.

The oxides i.e.,  $\text{MgO}$ ,  $\text{CoO}$ ,  $\text{NiO}$ ,  $\text{CuO}$ , and  $\text{ZnO}$  have different crystal structures as confirmed by XRD [27]. Accordingly, the crystal structure of  $\text{MgO}$ ,  $\text{CoO}$ , and  $\text{NiO}$  is a rock salt crystal structure while that of  $\text{CuO}$  and  $\text{ZnO}$  is the tenorite and Wurtzite structures, respectively. Since the crystal structure of the final product, HEO is a rock-salt structure,  $\text{MgO}$ ,  $\text{CoO}$ , and  $\text{NiO}$  remain in their original rock-salt structures. However, the  $\text{CuO}$  and  $\text{ZnO}$  must undergo crystal structure transition to the rock-salt from the tenorite and Wurtzite structures, respectively. The earlier works from the literature suggest that the mixing enthalpies ( $\Delta H_{\text{mix}}$ ) of the  $\text{ZnO}$  Wurtzite and  $\text{CuO}$  tenorite to their corresponding rock-salt crystal structure transformation are about 25 kJ/mol and 22 kJ/mol, respectively [47]. The positive  $\Delta H_{\text{mix}}$  indicates incomplete miscibility which leads to phase segregation at lower temperatures and can be stabilized at higher temperatures [48, 49] and this could be the main reason for detecting the tenorite and Wurtzite phases at lower temperatures.

To investigate the phase stability of the HEO powder calcined at 950 °C, the powder was uniaxially pressed into a pellet and subjected to sintering at a temperature of 1200 °C, followed by air quenching to room temperature. The obtained pellet was milled into a fine powder and characterized by XRD and compared to XRD of powder calcined at 950 °C as well as to that of the ball-milled (BM) powder as reported in Fig. 6. Comparing the XRD patterns of the powder calcined at 950 °C and the pellet sintered at 1200 °C, no secondary phase was observed in both samples and therefore, the materials remain stable in these temperature ranges.

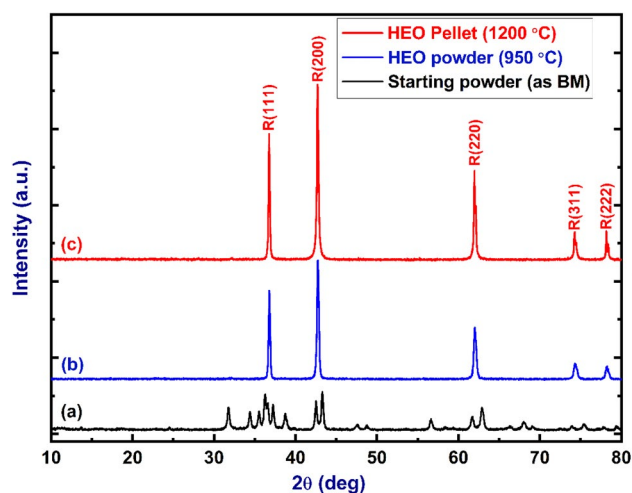


**Fig. 6** XRD patterns of (a) ball-milled (BM) powder, (b) HEO powder calcined at 950 °C, and (c) HEO pellet sintered at 1200 °C

Moreover, based on the effect of entropy on the phase stability of the system, the calculated maximum configurational entropy ( $\Delta S_{\text{config}}$ ) value of as-synthesized HEOs in an equiatomic five cations system was about  $1.61R$  per mole ( $\Delta S_{\text{config}} = 1.61R$ , according to Eq. 1), which is in agreement with the previously reported results [8, 20].

Pellets of the single-phase powder of HEO calcined at a temperature of  $950^\circ\text{C}$  were obtained by subjecting the powder to a uniaxial pressing, followed by sintering of the pellets in the temperature range from  $900$ – $1200^\circ\text{C}$ . Figure 7 (a–d) shows the fractured surface SEM micrograph of the pellets sintered at a temperature of  $900$ ,  $1000$ ,  $1100$ , and  $1200^\circ\text{C}$  for a constant sintering time of about 3 h. Figure 7 (a) shows that the sample sintered at  $900^\circ\text{C}$  is highly porous. It is evident that particles are sintered to some extent; however, the sample did not fully sinter due to the lack of enough sintering time which limits the diffusion of the particles. With increasing the sintering temperature, i.e., Fig. 7 (b, c, and d), relatively large particles are formed, in addition to the formation of necking of the particles which shows the start of the sintering process. Moreover, rod-shaped microstructural formations (red arrows on the microstructures) were observed within the sintering temperature ranges.

Figure 8 shows the effect of sintering temperature on the HEOs. Figure 8 (a) and (b) show the samples sintered at  $1100^\circ\text{C}$  for 3 h and 15 h, respectively. From the

micrographs, it is evident that increasing the sintering time resulted in a fully densified microstructure with well-defined grains and grain boundaries, Fig. 8 (b). Comparing Fig. 8 (a) and (b), the latter contains very few remaining open porosity that shows the full densification of the sample. The average grain size of the sample sintered at a temperature of  $1100^\circ\text{C}$  for 15 h of sintering time is about  $8\ \mu\text{m}$ .

The mechanical properties of ceramic materials depend on their microstructure, which is defined by the grain size, morphology, density, porosities, and porosity distribution as well as the chemical composition of the phases present [40]. In this work, the bulk densities ( $\rho_s$ ) of sintered pellets were determined using Archimedes' technique [50] and Table 2 presents the results of the sintered bulk densities of the sintered pellets. The densities of the sintered samples increased with increasing sintering temperature and time. To obtain the relative density ( $\rho_r$ ) of the samples, initially, the theoretical density ( $\rho_t$ ) was calculated for all solid solutions using their lattice parameters from the diffraction patterns of the relations  $\rho_t = (\text{cell mass}/\text{cell volume})$ , where the cell volume can be calculated from the lattice parameters obtained from the XRD diffraction results. Therefore, the calculated theoretical density of the single-phase HEO was about  $6.2\ \text{g}/\text{cm}^3$ . The relative density, which is given as  $\rho_r = (\rho_s/\rho_t)$ , was calculated and provided in Table 2.

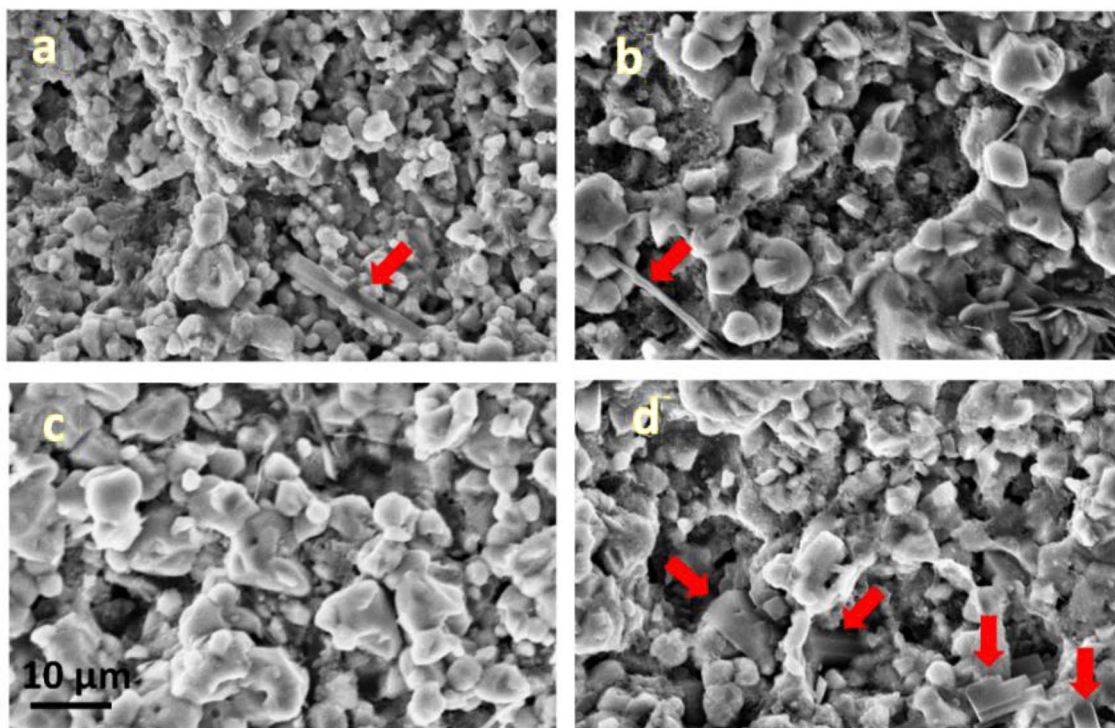
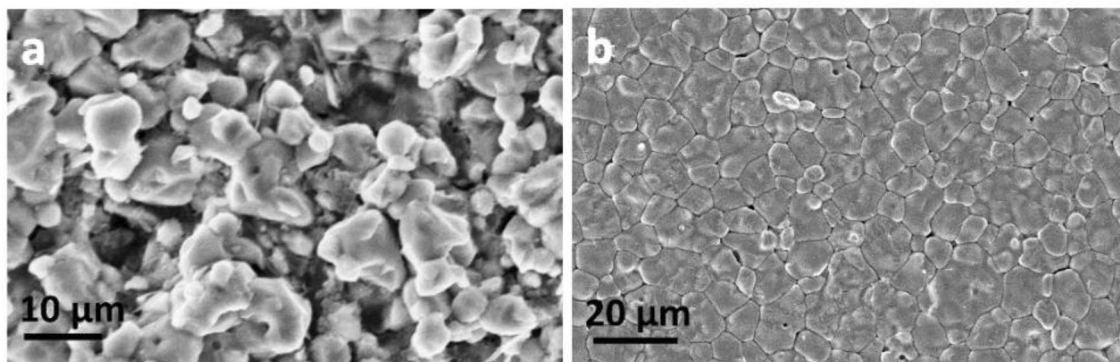


Fig. 7 SEM micrographs of HEO samples sintered at (a)  $900^\circ\text{C}$ , (b)  $1000^\circ\text{C}$ , (c)  $1100^\circ\text{C}$ , and  $1200^\circ\text{C}$  for a sintering time of 3 h



**Fig. 8** SEM micrographs of HEO samples sintered at 1100 °C with sintering time of (a) 3 h and (b) 15 h

**Table 2** Sintered densities of pellets of the HEOs at different sintering temperatures and times

Sintering Temperature (°C)	900	1000	1100	1200	1100	1100	1200	1200
Sintering Time (h)	3	3	3	3	9	15	9	15
Sintered bulk density, $\rho_s$ (g/cm <sup>3</sup> )	4.272	4.774	4.822	5.027	5.568	5.800	5.954	6.116
Relative density, $\rho_r$ (%)	69.28	77.42	78.20	81.52	90.30	94.06	96.56	99.20

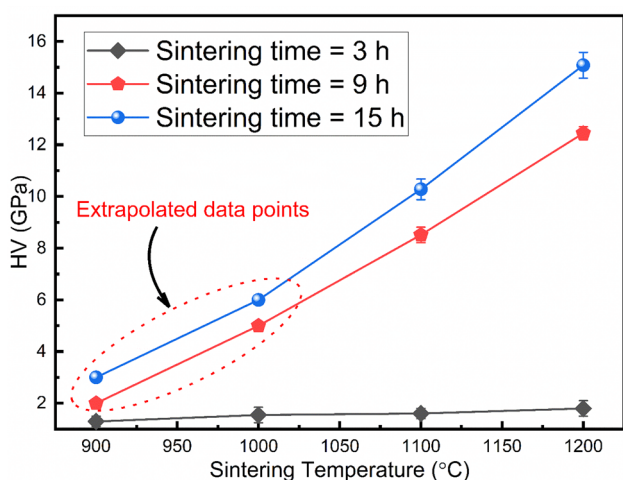


**Fig. 9** A plot showing the Vickers hardness of the HEOs sintered at different sintering times within the temperature range from 900–1200 °C

The mechanical property of the sintered samples was investigated using Vickers hardness (HV), which is given as  $HV = 1.8544(F/D^2)$ , where  $F$  is the applied load measured in kilograms-force (kgf) given as a ratio of the maximum load ( $P$ ) applied to the specimen (kN) and cross-sectional area ( $A$ ) of the specimen (mm<sup>2</sup>) and  $D$  is the mean diagonals of impression (mm). The results of the HV of the samples sintered at different temperatures and times are provided in Fig. 9.

Figure 9 shows that the value of the HV increased with increasing the sintering temperature and time, reaching

a value of about 16 GPa, which is in close agreement with the results of the microstructures of Figs. 7 and 8. The average hardness of the individual oxides, i.e., CuO, NiO, ZnO, CoO, and MgO is 0.25 GPa[51], 6.1 GPa[9], 2.1 GPa [52, 53], 2.8 GPa[9], and 8.4 GPa[9], respectively. The sintered HEO pellets showed higher values of Vickers hardness compared to the values of the average hardness of the individual oxides. Moreover, a comparison was made to the literature values of some of the hard ceramic materials on their hardness values. For instance, the hardness of dense alumina ( $\alpha$ -Al<sub>2</sub>O<sub>3</sub>) ceramic material ranges from about 15–20 GPa while that of the SiC is about 25 GPa [54, 55]. Therefore, the hardness values obtained in the present work are comparable to that of the hard ceramic materials, and these results can be further enhanced if the synthesis methodologies can be further investigated.

### 4 Conclusions

In this work, binary oxides of MgO, CoO, NiO, CuO, and ZnO were successfully synthesized through co-precipitation methods. From these binary oxide ceramic materials, the HEO system was synthesized using the solid-state reaction method, followed by both the binary oxides and the HEO characterizations. From the phase purity and structural analysis, the single-phase and rock-salt crystal structure of the HEO was achieved above a calcination temperature of 950 °C. The microstructure and morphology of the sintered samples exhibited a considerable grain growth with increasing sintering temperatures



and times and well-defined grains and grain boundaries were developed with minimum porosity at a sintering temperature of 1200 °C for 15 h of sintering time. The sample subjected to these sintering conditions showed a relative bulk density and Vickers hardness of about 99% and 16 GPa, respectively, which is comparable with some of the hard ceramic materials reported in the literature. Therefore, this class of new ceramic materials could be a potential candidate for structural applications if the processing conditions are further optimized.

**Acknowledgements** The authors acknowledge the financial support provided by Adama Science and Technology University (ASTU). Moreover, Mr. Demeke Tesfaye from the Department of Materials Science and Engineering, ASTU, is strongly acknowledged for his support in conducting some of the experimental works.

## Declarations

**Conflict of interest** The authors declare that they have no competing interest.

**Open Access** This article is licensed under a Creative Commons Attribution 4.0 International License, which permits use, sharing, adaptation, distribution and reproduction in any medium or format, as long as you give appropriate credit to the original author(s) and the source, provide a link to the Creative Commons licence, and indicate if changes were made. The images or other third party material in this article are included in the article's Creative Commons licence, unless indicated otherwise in a credit line to the material. If material is not included in the article's Creative Commons licence and your intended use is not permitted by statutory regulation or exceeds the permitted use, you will need to obtain permission directly from the copyright holder. To view a copy of this licence, visit <http://creativecommons.org/licenses/by/4.0/>.

## References

1. Dai W, Lu T, Pan Y (2019) Novel and promising electrocatalyst for oxygen evolution reaction based on MnFeCoNi high entropy alloy. *J Power Sour* 430:104–111
2. Miracle DB, Senkov ON (2017) A critical review of high entropy alloys and related concepts. *Acta Mater* 122:448–511
3. Miracle D et al (2014) Exploration and development of high entropy alloys for structural applications. *Entropy* 16(1):494–525
4. Yeh J-W et al (2004) Nanostructured high-entropy alloys with multiple principal elements: novel alloy design concepts and outcomes. *Adv Eng Mater* 6(5):299–303
5. Yeh JW et al (2007) High-entropy alloys – a new era of exploitation. *Mater Sci Forum* 560:1–9
6. Fu M et al (2021) High-entropy materials for energy-related applications. *iScience* 24(3): 102177
7. Zhang Y (2019) High-Entropy Materials, Overview of High-Entropy Alloys, Springer, Singapore [https://doi.org/10.1007/978-3-319-27013-5\\_1](https://doi.org/10.1007/978-3-319-27013-5_1)
8. Yeh J-W (2016) Overview of High-Entropy Alloys. Overview of High-Entropy Alloys. Springer, Cham, [https://doi.org/10.1007/978-3-319-27013-5\\_1](https://doi.org/10.1007/978-3-319-27013-5_1)
9. Rost CM et al (2015) Entropy-stabilized oxides. *Nat Commun* 6:8485
10. Dusza J et al (2018) Microstructure of (Hf-Ta-Zr-Nb)C high-entropy carbide at micro and nano/atomic level. *J Eur Ceram Soc* 38(12):4303–4307
11. Tsai D-C et al (2013) Structural morphology and characterization of (AlCrMoTaTi)N coating deposited via magnetron sputtering. *Appl Surf Sci* 282:789–797
12. Guan J et al (2020) Synthesis and thermal stability of novel high-entropy metal boron carbonitride ceramic powders. *Ceram Int*, <https://doi.org/10.1016/j.ceramint.2020.07.126>
13. Zhang R-Z, Reece MJ (2019) Review of high entropy ceramics: design, synthesis, structure and properties. *J Mater Chem A* 7(39):22148–22162
14. Sarkar A et al (2018) Rare earth and transition metal based entropy stabilised perovskite type oxides. *J Eur Ceram Soc* 38(5):2318–2327
15. Glasscott MW et al (2019) Electrosynthesis of high-entropy metallic glass nanoparticles for designer, multi-functional electrocatalysis. *Nat Commun* 10(1):2650
16. Desissa TD (2021) NiO–ZnO based junction interface as high-temperature contact materials. *Ceram Int* 47(6):8053–8059
17. Desalegn YM, Andoshe DM, Desissa TDJMRE (2020) Composite of bentonite/CoFe<sub>2</sub>O<sub>4</sub>/hydroxyapatite for adsorption of Pb (II). *Mater Res Express* <https://doi.org/10.1088/2053-1591/abc71f>
18. Khan MM, Adil SF, Al-Mayouf A (2015) Metal oxides as photocatalysts. *J Saudi Chem Soc* 19(5):462–464
19. Elumalai NK et al (2015) Metal oxide semiconducting interfacial layers for photovoltaic and photocatalytic applications. *Mater Renew Sustainable Energy* 4(3):11
20. Lorenz M et al (2016) The 2016 oxide electronic materials and oxide interfaces roadmap. *J Physics D: Appl Phys* 49(43): 433001
21. McCormack SJ, Navrotsky AJAM (2021) Thermodynamics of high entropy oxides. *Acta Mater* 202:1–21
22. Sarkar A et al (2019) High-Entropy Oxides: Fundamental Aspects and Electrochemical Properties. *Adv Mater* 31(26): e1806236
23. Dupuy A, Wang X, Schoenung J (2019) Entropic phase transformation in nanocrystalline high entropy oxides. *Mater Res Letters* 7:60–67
24. Zhang Y et al (2014) Microstructures and properties of high-entropy alloys. *Prog Mater Sci* 61:1–93
25. Biesuz M et al (2018) Synthesis and sintering of (Mg Co, Ni, Cu, Zn)O entropy-stabilized oxides obtained by wet chemical methods. *J Mater Sci* 53(11):8074–8085
26. Sarkar A, Breitung B, Hahn H (2020) High entropy oxides: The role of entropy, enthalpy and synergy. *Scripta Mater* 187:43–48
27. Pickering EJ, Jones NG (2016) High-entropy alloys: a critical assessment of their founding principles and future prospects. *Int Mater Rev* 61(3):183–202
28. Parida T et al (2020) Novel rare-earth and transition metal-based entropy stabilized oxides with spinel structure. *Scripta Mater* 178:513–517
29. Sarkar A et al (2017) Nanocrystalline multicomponent entropy stabilised transition metal oxides. *J Eur Ceram Soc* 37(2):747–754
30. Banerjee R et al (2020) High-entropy Perovskites: an emergent class of oxide thermoelectrics with ultralow thermal conductivity. *ACS Sustain Chemi Engi* 8(46):17022–17032
31. Edalati P et al (2020) Photocatalytic hydrogen evolution on a high-entropy oxide. *J Mater Chem A* 8(7):3814–3821
32. Bérardan D et al (2016) Colossal dielectric constant in high entropy oxides. *physica status solidi (RRL) - Rapid Research Letters*, 10(4): 328–333
33. Wang Q et al (2019) High entropy oxides as anode material for Li-ion battery applications: a practical approach. *Electrochem Commun* 100:121–125

34. Aziz BK, Karim MAH (2019) Efficient catalytic photodegradation of methylene blue from medical lab wastewater using MgO nanoparticles synthesized by direct precipitation method. *React Kinet Mech Catal* 128(2):1127–1139
35. Ravi Dhas C et al (2015) Visible light driven photocatalytic degradation of Rhodamine B and Direct Red using cobalt oxide nanoparticles. *Ceram Int* 41(8):9301–9313
36. Manouchehri I, Kameli P, Salamati H (2011) Facile synthesis of Co<sub>3</sub>O<sub>4</sub>/CoO nanoparticles by thermal treatment of ball-milled Precursors. *J Supercond Novel Magn* 24(6):1907–1910
37. Vijaya Kumar P, Jafar Ahamed A, Karthikeyan M (2019) Synthesis and characterization of NiO nanoparticles by chemical as well as green routes and their comparisons with respect to cytotoxic effect and toxicity studies in microbial and MCF-7 cancer cell models. *SN Appl Sci* <https://doi.org/10.1007/s42452-019-1113-0>
38. Phiw dang K et al (2013) Synthesis of CuO nanoparticles by precipitation method using different precursors. *Energy Procedia* 34:740–745
39. Wasly HS, El-Sadek MSA, Batoor KM (2019) Novel synthesis, structural, optical properties and antibacterial activity of ZnO nanoparticles. *Mater Res Express* 6(5): 055003
40. Rost C et al (2017) Local structure of the Mg<sub>x</sub>Ni<sub>x</sub>Co<sub>x</sub>Cu<sub>x</sub>Zn<sub>x</sub>O(x=0.2) entropy-stabilized oxide: an EXAFS study. *J Am Ceram Soc* 100(6): 2732–2738
41. Qiu N et al (2019) A high entropy oxide (Mg<sub>0.2</sub>Co<sub>0.2</sub>Ni<sub>0.2</sub>Cu<sub>0.2</sub>Zn<sub>0.2</sub>O) with superior lithium storage performance. *J Alloys Compounds* 777: 767–774
42. Mofokeng SJ et al (2020) Thermoluminescence properties of MgO:Al<sup>3+</sup>, Li<sup>+</sup> prepared by microwave-assisted solution combustion method. *Physica B: Condensed Matter* 582: 412008
43. Mirzaei H et al (2018) Direct growth of ternary copper nickel cobalt oxide nanowires as binder-free electrode on carbon cloth for nonenzymatic glucose sensing. *Microchem J* 142:343–351
44. Nguyen K et al (2018) A comparative study on the electrochemical properties of nanoporous nickel oxide nanowires and nanosheets prepared by a hydrothermal method. *RSC Adv* 8:19449–19455
45. Sathyanathan S, Sivakumaran K, Jayamoorthy K (2016) FTIR and multivariate analysis to study the effect of bulk and nano copper oxide on peanut plant leaves. *J Sci: Adv Mater Devices* <https://doi.org/10.1016/j.microc.2018.07.014>
46. Arefi M, Rezaei-Zarchi S (2012) Synthesis of zinc oxide nanoparticles and their effect on the compressive strength and setting time of self-compacted concrete paste as cementitious composites. *Int J Mol Sci* 13:4340–4350
47. Khadivi Ayask H, Vahdati Khaki J, Haddad Sabzevar M (2015) Facile synthesis of copper oxide nanoparticles using copper hydroxide by mechanochemical process. *J Ultrafine Grained Nanostr Mater* 48(1): 110–112
48. El-Shobaky GA et al (1996) Thermal decomposition of basic cobalt and copper carbonates. *J Therm Anal* 46(6):1801–1808
49. Davies PK, Navrotsky A (1981) Thermodynamics of solid solution formation in NiO-MgO and NiO-ZnO. *J Solid State Chem* 38(2):264–276
50. Mayrhofer PH et al (2018) High-entropy ceramic thin films; A case study on transition metal diborides. *Scripta Mater* 149:93–97
51. Lužnik J et al (2015) Complex magnetism of Ho-Dy-Y-Gd-Tb hexagonal high-entropy alloy. *Phys Rev B* <https://doi.org/10.1103/PhysRevB.92.224201>
52. ASTM C20 - 00(2010) Standard test methods for apparent porosity, water absorption, apparent specific gravity, and bulk density of burned refractory brick and shapes by boiling water. *ASTM Int*
53. Kreuzeder M et al (2015) Fabrication and thermo-mechanical behavior of ultra-fine porous copper. *J Mater Sci* 50(2):634–643
54. Giberteau F et al (1982) Deformation of MgO by Vickers microindentation tests, *Revue de Physique Appliquée* 17(12) 777–782
55. Yoshimura HN et al (2006) Mechanical properties and microstructure of zinc oxide varistor ceramics. *Mater Sci Forum* 530–531:408–413

**Publisher's Note** Springer Nature remains neutral with regard to jurisdictional claims in published maps and institutional affiliations.